


## Programmable Superconducting Processor with Native Three-Qubit Gates

Tanay Roy,<sup>†</sup> Sumeru Hazra, Suman Kundu, Madhavi Chand, Meghan P. Patankar, and R. Vijay\*  
*Department of Condensed Matter Physics and Materials Science, Tata Institute of Fundamental Research,  
 Homi Bhabha Road, Mumbai 400005, India*

 (Received 16 January 2020; revised 24 January 2020; accepted 22 May 2020; published 23 July 2020)

Superconducting circuits are at the forefront of quantum-computing technology because of the unparalleled combination of good coherence, fast gates, and flexibility in design parameters. The majority of experiments demonstrating small quantum algorithms in the superconducting architecture have used transmon qubits, which are coupled via capacitors or microwave cavities. Apart from coherence and gate fidelity, two important factors that currently limit the performance of a superconducting processor are nearest-neighbor interqubit coupling (in one or two dimensions) and being restricted to two-qubit entangling gates only. In this work, we present a programmable three-qubit processor circuit, nicknamed “trimon,” with strong all-to-all coupling and access to native three-qubit gates. We benchmark our processor by implementing a three-qubit version of various algorithms, namely Deutsch-Jozsa, Bernstein-Vazirani, Grover’s search and the quantum Fourier transform. In particular, we note that the native three-qubit controlled operations enable our ancilla-free implementation of Grover’s algorithm to outperform previous demonstrations. Our results clearly show the advantage of having native three-qubit gates, and that can play a crucial role in improving the performance of larger systems having the trimon as a building block.

DOI: [10.1103/PhysRevApplied.14.014072](https://doi.org/10.1103/PhysRevApplied.14.014072)

### I. INTRODUCTION

Quantum computing offers extraordinary capabilities at solving certain problems by taking classically inaccessible paths. A full-fledged quantum computer, apart from a robust, scalable architecture, will benefit from error-correcting codes to prevent irreversible losses arising due to decoherence [1]. Although multiple theories for quantum error correction have emerged, experimental realizations have remained extremely challenging due to stringent conditions on qubit coherence, control, and connectivity. Given these constraints, a significant effort is focused on building moderate-sized processors [2–5] with the hope that these noisy quantum computers [6] might outperform today’s classical digital computers for some selected tasks. Without error correction, the only way to boost performance is to improve gate fidelity, maximize interqubit connectivity, and incorporate native higher-dimensional ( $>2$ ) gates.

A universal quantum-computing platform can be constructed using controlled-NOT (CNOT) (or controlled-phase) gates along with single-qubit rotations [7]. Nevertheless, interactions beyond two qubits play an important role in

realizing efficient quantum hardware by simplifying complex sequences of two-qubit gates. While specific quantum algorithms have been demonstrated on several quantum-computing platforms [8–20], universally programmable processors have only been built recently [2,3,5,21,22]. However, they have been limited to two-qubit gates native to those systems, requiring a longer sequence of gates and thus limiting their implementation efficiency. One important three-qubit gate that can significantly improve this efficiency is the Toffoli gate [23], which flips the state of the target qubit conditioned upon the state of the two control qubits. Together with single-qubit gates, it also forms a universal set for quantum computation [24]. Although the Toffoli gate has been implemented in various architectures, so far all of them require multiple pulses [25–31] due to the nonavailability of a native three-qubit gate. Recently, higher-dimensional operations in superconducting circuits have been explored using native many-body interactions [32,33] or through pairwise interactions in highly connected qubit networks [34,35]. However, no quantum algorithms have been implemented using these architectures yet.

In this work, we present a three-qubit quantum processor based on multimode superconducting circuits with *all-to-all* connectivity between the qubits and a native high-fidelity three-qubit gate. The processor, nicknamed “trimon,” can perform universal quantum computation through execution of a sequence of logic gates completely

\*r.vijay@tifr.res.in

<sup>†</sup>Current address: Department of Physics and James Franck Institute, University of Chicago, Chicago, Illinois 60637, USA.

programmable in software. The native gates in our system are the generalized controlled-controlled-rotations, which we achieve with an unprecedented mean fidelity of about 99%. We demonstrate a range of three-qubit quantum algorithms using an efficient implementation made possible by access to *near-perfect* generalized controlled-controlled-phase gates [36]. As examples, Deutsch-Jozsa [37], Bernstein-Vazirani [38], and Grover’s search [39] algorithms show success probabilities of 92, 63, and 49% respectively, significantly larger than the corresponding classical bounds (see Appendix A) of 50, 25, and 25%. We also demonstrate the quantum Fourier transform [1] to estimate phase and amplitude modulation of different three-qubit states.

## II. TRIMON

### A. System Hamiltonian

Our system consists of a modified version of the previously introduced “trimon” device [40] optimized for three-qubit operations. A scanning electron micrograph of a device nominally identical to the one used in the experiments is shown in Fig. 1. The capacitor pads are made unequal and are placed asymmetrically to achieve the desired asymmetry for optimal level spacing and coupling strengths [36] (see Appendix B). The pads are connected to the nodes of a ring with four superconducting arms. Two diagonally opposite arms contain SQUIDs and the

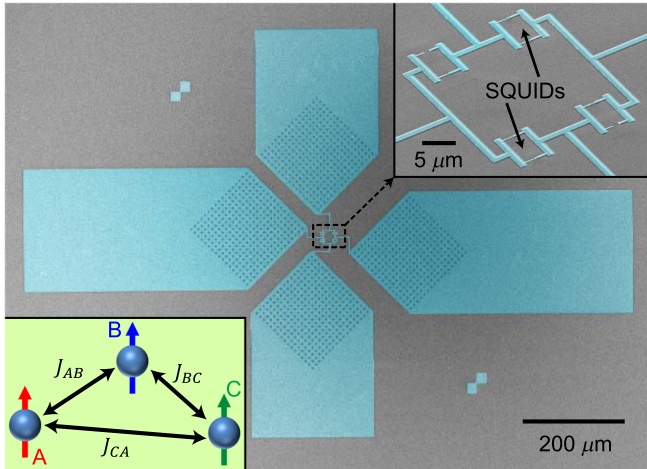


FIG. 1. False colored scanning electron micrograph of the trimon device in three-dimensional (3D) geometry. The capacitor pads are placed asymmetrically to achieve optimal level spacing. The waffle pattern close to the junctions is meant for flux trapping. The top-right inset shows an enlarged view of the junction area, where two diagonally opposite junctions are replaced with superconducting quantum interference devices (SQUIDs) for *in situ* tunability of the junction asymmetry. The trimon can be described as a system of three transmonlike qubits with strong cross-Kerr coupling as depicted in the bottom-left inset.

remaining two contain single Josephson junctions (top-right inset of Fig. 1) to control junction asymmetry *in situ* and tune level spacing. The device gives rise to three coupled anharmonic oscillator modes (labeled A, B, and C) each of which behaves as a transmon [41] qubit. The nonlinearity in the system provides the pairwise intermode cross-Kerr coupling [40] (bottom-left inset of Fig. 1) and the Hamiltonian of the system coupled dispersively to a host readout cavity can be expressed as

$$\begin{aligned} \frac{1}{\hbar} H_{\text{disp}} = & \sum_{\mu=A,B,C} [(\omega_{\mu} - \beta_{\mu})\hat{n}_{\mu} - J_{\mu}(\hat{n}_{\mu})^2] \\ & - \sum_{\mu \neq \nu} 2J_{\mu\nu}\hat{n}_{\mu}\hat{n}_{\nu} + \omega_r \left( \hat{n}_r + \frac{1}{2} \right) \\ & + 2\chi(\hat{n}_A, \hat{n}_B, \hat{n}_C)\hat{n}_r, \end{aligned} \quad (1)$$

where  $\omega_{\mu=A,B,C}$  are the mode frequencies in the absence of any nonlinearity (and hence coupling),  $\beta_{\mu} = J_{\mu} + \sum_{\nu \neq \mu} J_{\mu\nu}$  are the shifts due to self-Kerr- ( $J_{\mu}$ ) and cross-Kerr- ( $J_{\mu\nu}$ ) type nonlinearities,  $\hat{n}_{\mu}$  is the photon number operator for the  $\mu$ th mode,  $\hat{n}_r$  is the cavity’s photon number operator, and  $\chi$  is the occupation-dependent dispersive shift [36].

The computational subspace of the system is composed of zero and single-excitation states of each mode [Fig. 2(a)] so that this subspace can be described as either an eight-dimensional Hilbert space or a composite three-qubit system. The first picture depicts the presence of eight energy eigenstates with specific selection rules for the allowed transitions whereas the second picture depicts three qubits whose transition frequencies are dependent on the state of the partner qubits [dashed boxes of Fig. 2(a) for qubit C]. In what follows, we stick to the second picture. Each qubit thus has four distinct transition frequencies determined by the interqubit coupling strengths, totaling 12 transitions for the whole system. However, one does not need individual microwave sources to address all the transitions, since frequencies for a single qubit are within a window narrow enough to be generated comfortably from a single source using sideband modulation techniques.

### B. Gate operations

A microwave drive at each of the 12 transitions implements a controlled-controlled-rotation  $CCR(\phi, \theta)$ , where  $\phi$  is the azimuthal angle with respect to the  $y$  axis and  $\theta$  is the polar angle of the Bloch sphere comprising of the two levels connected by the specific transition. The four dashed boxes in Fig. 2(a) show circuit representations for different  $CCR(\phi, \theta)$  gates on qubit C. A  $\pi$  pulse about the  $x$  axis,  $CCR(-\pi/2, \pi)$ , along with appropriate phase shifts of the following pulses [36,40] then implements a CCNOT or Toffoli gate. Two-qubit CNOT gates can then be decomposed into two such CCNOT gates and effective

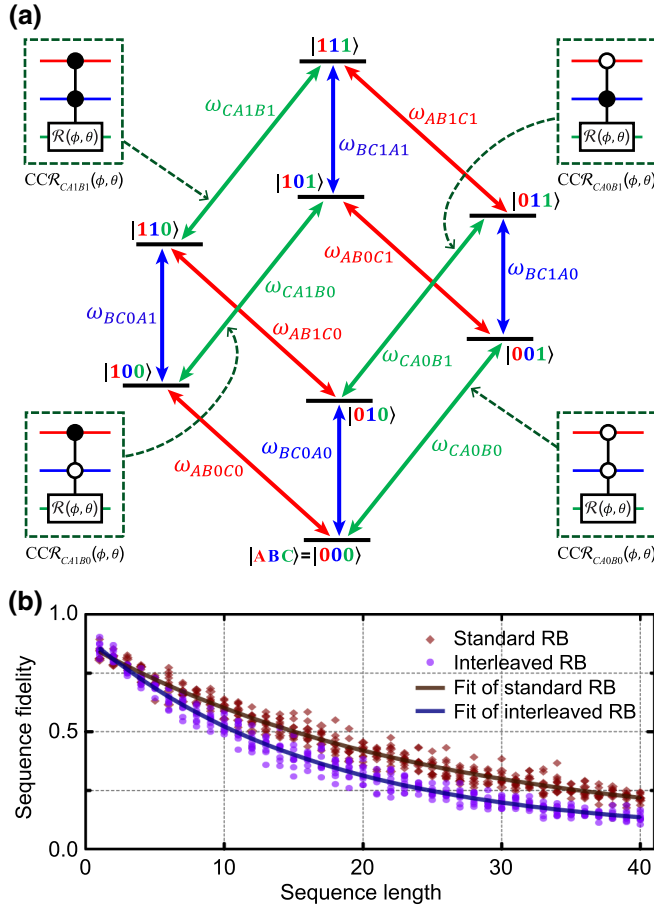


FIG. 2. Level diagram and randomized benchmarking. (a) Computational subspace of the trimon consisting of eight energy eigenstates connected through 12 transitions. The trimon can be described as either an eight-level system or a three-qubit system where each qubit has four transition frequencies dependent on the state of its partners. Each transition allows implementation of controlled-controlled-rotation  $[CCR(\phi, \theta)]$  through application of a microwave drive. Four  $CCR(\phi, \theta)$  gates for qubit C are shown inside the dashed boxes. (b) Standard (brown) and interleaved (blue) RB at the transition CA1B1. Each RB sequence is preceded by two  $\pi$  pulses at  $\omega_{AB0C0}$  and  $\omega_{BC0A1}$  to initialize the system in the  $|110\rangle$  state. Sequence fidelity is obtained by applying the same  $\pi$  pulses in reverse order after the RB sequence and measuring the population in the  $|000\rangle$  state. Interleaved RB is performed for the  $\pi$  pulse at  $\omega_{CA1B1}$ , which is equivalent to a Toffoli gate (with appropriate phase advancement). In total, ten randomized sequences are applied for every sequence length and each data point is a result of averaging 30 000 experimental runs. The solid lines correspond to fits from which gate fidelities are extracted.

single-qubit rotations  $\mathcal{R}(\phi, \theta)$  require application of all four  $CCR(\phi, \theta)$  gates. Another interesting feature of the trimon is the ability to implement a *near-perfect generalized arbitrary* controlled-controlled-phase  $[CC\theta(\theta)]$  gate. These gates are realized by appropriately shifting the phase of all subsequent pulses connecting the particular basis

on which the gate is intended to be applied [36]. Consequently, these  $CC\theta(\theta)$  gates are of zero duration and can be considered as virtual gates [42]. The *near-perfect* aspect comes from the fact that decoherence of the qubits has no effect on these gates and the required phase-shifted waveforms are generated in software, which can be done with extreme precision (barring any digitization error). Further, *generalized* indicates the possibility of any combination of  $|0\rangle$  or  $|1\rangle$  as controls and *arbitrary* signifies shifting the phase by an arbitrary amount  $\theta$ . Controlled-controlled-Z gate, which flips the phase of a particular basis component, then becomes a special case:  $CCZ = CC\theta(\pi)$ . Using the  $CCR(\phi, \theta)$  and  $CC\theta(\theta)$  gates, arbitrary three-qubit unitary operations can be implemented on our system.

### III. EXPERIMENT

#### A. Device characterization

An experiment on the trimon begins with the determination of the transition frequencies done using standard two-tone spectroscopy with one or two prior  $\pi$  pulses for state initialization as one moves up in the ladder [Fig. 2(a)]. The  $TE_{101}$  mode (with resonance at  $\omega_r/2\pi = 7.2742$  GHz and bandwidth  $\kappa/2\pi = 3.3$  MHz) of a 3D rectangular copper cavity is used for the joint dispersive measurement [13,43–45] of the three qubits. Transitions to the second excited states of each mode are also determined using this technique (while keeping the other two qubits in their ground states) and cross verified by the two-photon transitions from the ground states. Measurement of these 15 transitions allows determination of the anharmonicities ( $-2J_\mu$ ) and interqubit coupling ( $J_{\mu\nu}$ ) strengths. Then coherence measurements on the three transitions involving zero- to single-photon excited states [bottom three transitions in Fig. 2(a):  $\omega_{\mu=A,B,C}^{00}$ ] of each mode are performed to characterize the qubits. Dispersive shifts of the qubits are determined by measuring the shift in cavity frequency when the qubits are excited to the first excited state individually. All three qubits have well separated frequencies, long coherence times, moderate anharmonicities, and strong interqubit coupling. These results are summarized in Table I.

#### B. Gate fidelity

Next, we characterize our native  $CCR(\phi, \theta)$  gates by adapting the standard and interleaved randomized benchmarking (RB) protocols [46,47]. (see Appendix D). We replace the two levels of a conventional qubit with two basis states connected by the transition addressed [see Fig. 2(a)] and thus we call our technique transition-selective RB. Generation of the required 12 tones is done using three microwave sources where each source is modulated to create four frequencies for a single

TABLE I. Parameters and coherence properties of the trimon device. The transition frequency  $\omega^{00}$  of each qubit with the other two qubits in their ground states is listed along with the anharmonicity ( $-2J_\mu$ ), the relaxation time ( $T_1^{00}$ ), the Ramsey decay constant ( $T_{\text{Ram}}^{00}$ ), the dispersive shift ( $\chi$ ), and the interqubit coupling strength ( $J_{\mu\nu}$ ).

Qubit	$\omega^{00}/2\pi$ (GHz)	$-J_\mu/\pi$ (MHz)	$T_1^{00}$ ( $\mu\text{s}$ )	$T_{\text{Ram}}^{00}$ ( $\mu\text{s}$ )	$\chi/2\pi$ (MHz)	$J_{\mu\nu}/\pi$ (MHz)
A	4.9278	-107.9	43.7	38.9	-0.064	$J_{AB}/\pi = 192.4$
B	4.5146	-113.1	43.5	43.3	-0.061	$J_{BC}/\pi = 211.4$
C	5.6864	-138.0	26.3	13.6	-0.069	$J_{CA}/\pi = 242.0$

qubit. Transition-selective standard RB of each transition involves a sequence of computational gates chosen randomly from the Clifford operators involving the two specific basis states. To determine the fidelity of a particular gate we perform interleaved RB by inserting that gate after every computational gate in a standard RB sequence. Figure 2(b) shows standard and interleaved RB data for the transition  $\omega_{CA1B1}$ . The average gate fidelity  $\mathcal{F}_{\text{avg}}$  obtained from standard RB and  $\pi$ -gate (Toffoli) fidelity  $\mathcal{F}_\pi$  obtained from interleaved RB, along with gate lengths, for all 12 transitions are shown in Table III. The average of  $\mathcal{F}_\pi$  across all transitions is found to be 99.1(1)%. Fidelities of any two-qubit or single-qubit gates can be estimated by taking products of fidelities of the constituent  $CCR(\phi, \theta)$  gates.

### C. Deutsch-Jozsa algorithm

In order to demonstrate the universal programmability of our processor and characterize its performance, we run various three-qubit quantum algorithms. We start with the Deutsch-Jozsa (DJ) algorithm [37], a simple quantum algorithm to show quantum advantage over classical methods. The DJ algorithm determines whether a function  $f$  (also called the ‘‘oracle’’) is balanced or constant. The function takes an  $n$ -bit register  $\mathbf{x}$  as input and is said to be balanced if the one-bit output is 0 for exactly half of the possible inputs and 1 for the rest, whereas  $f$  is called a constant function if the output is always 0 or 1 irrespective of the input. In the classical case one needs 2 (best scenario) to  $2^{n-1} + 1$  (worst scenario) evaluations to determine the nature of the function, whereas the quantum algorithm requires only one evaluation.

Figure 3 shows the quantum circuit for our (*ancilla-free*) implementation of the DJ algorithm. The algorithm starts with preparation of a specific equal superposition state  $(|0\rangle + |1\rangle)(|0\rangle + |1\rangle)(|0\rangle - |1\rangle)/2\sqrt{2}$  using  $\pm Y_{\pi/2}$  gates [positive or negative rotation about the  $y$  axis by an amount  $\pi/2$ , which are composed of four  $CCR(0, \pi/2)$  pulses]. We implement the constant function by either applying or not applying an  $X_\pi$  gate ( $\pi$  rotation about the  $x$  axis) on qubit C, which corresponds to  $f(x) = 1$  and 0, respectively (see Fig. 3). Ten different kinds of balanced functions are implemented by applying a combination of  $Z_\pi$  and controlled- $Z$  gates. After application of one of the oracles,

the states are rotated back before the final measurement. A final outcome of  $|000\rangle$  indicates a constant function whereas anything else implies a balanced function. We obtain mean success probabilities of 95.5(1) and 79.3(3)% for the balanced and constant functions respectively, with theoretical predictions being 100% for both cases. None of the algorithmic outcomes are corrected for state preparation and measurement (SPAM) errors. Individual success probabilities for all the functions are tabulated in Table II and indicate somewhat poorer performance than previous demonstrations in a three-qubit NMR [48] and a five-qubit trapped-ion system [2].

### D. Bernstein-Vazirani algorithm

The Bernstein-Vazirani (BV) [38] algorithm is similar to the DJ algorithm, where the goal is to determine an unknown string of binaries  $\mathbf{c} = \{c_1, c_2, \dots, c_n\}$ . The oracle is defined as  $\mathbf{c} \cdot \mathbf{x} \bmod 2$ , where  $\mathbf{x}$  is the input register which the user can control. The BV algorithm just takes one execution of the oracle to find the unknown string  $\mathbf{c}$ . The quantum circuit and results are shown in Fig. 4(a). The eight instances of the oracle are implemented by the application of conventional  $CNOT_{A \rightarrow C}$ ,  $CNOT_{B \rightarrow C}$  (each composed of two  $CCNOT$ ) and  $Y_\pi$  [composed of four  $CCR(0, \pi)$ ] gates on qubit C conditioned on the classical bits being 1 in the unknown string. The results are shown in Fig. 4(a). On average, correct results are obtained with a probability of 63.1(3)%, which is not as good as previous demonstrations

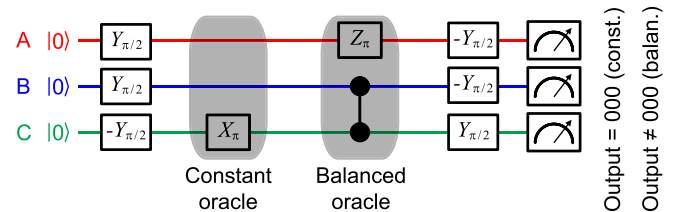


FIG. 3. Quantum circuit for the Deutsch-Jozsa algorithm.  $W_\theta$  ( $-W_\theta$ ) represents a positive (negative) rotation about the  $w$  axis by an amount  $\theta$ . The oracle is implemented through the application of gates in one of the shaded regions. The constant function is implemented by the presence or absence of the  $X_\pi$  gate on qubit C. An example ( $A \oplus BC$ ) for the balanced function is shown. A measurement output of  $|000\rangle$  indicates a constant function.

TABLE II. Results of the three-qubit Deutsch-Jozsa algorithm. The success probabilities (SPs) for the two implementations of the constant function [ $f(x) = 0$  or  $1$ ] and ten different implementations of the balanced function are shown. The theoretical success probabilities are 100% for all the cases. The numbers in parentheses represent standard error obtained after 20 000 repetitions of each oracle.

Function	Constant		Balanced									
	0	1	A	B	C	$A \oplus B$	$B \oplus C$	$C \oplus A$	$A \oplus BC$	$B \oplus CA$	$C \oplus AB$	$AB \oplus BC \oplus CA$
SP(%)	86.0(3)	72.6(3)	93.4(2)	92.2(2)	94.9(2)	97.4(1)	98.1(1)	97.5(1)	96.9(1)	96.0(1)	95.0(2)	93.5(2)

in optical and trapped-ion systems [2,4,11]. However, as we see next, the true power of the processor is revealed in algorithms where native three-qubit gates are needed.

### E. Grover's search algorithm

The DJ and BV algorithms are deterministic in nature. However, there are certain quantum algorithms that find the correct answer probabilistically and yet provide quantum advantage. Next, we demonstrate one such algorithm, namely Grover's algorithm [39], which can provide quadratic speedup in searching an unsorted database. This algorithm can find, in  $O(\sqrt{N})$  steps, the unique input that produces a specific output when fed to a database of size  $N$ . We perform a single iteration of Grover's search on

our three-qubit system with database size  $N = 2^3 = 8$ . The theoretical probability of getting the right answer after a single iteration of Grover's algorithm for  $N = 8$  is 78.125% [49], compared to 25% for the classical case [21]. Our implementation of the quantum circuit is shown in Fig. 4(b), which does not require any ancillary qubit. The algorithm starts with preparation of the equal superposition state  $(|0\rangle + |1\rangle)(|0\rangle + |1\rangle)(|0\rangle + |1\rangle)/2\sqrt{2}$ , realized by  $Y_{\pi/2}$  gates on all qubits, followed by the mapping of the marked state through an oracle, which we implement using appropriate CCZ gates. The oracle flips the probability amplitude of the marked state, which is then amplified by the next stage of operations [gates within the dashed lines in Fig. 4(b)]. Finally, the qubits are measured to find

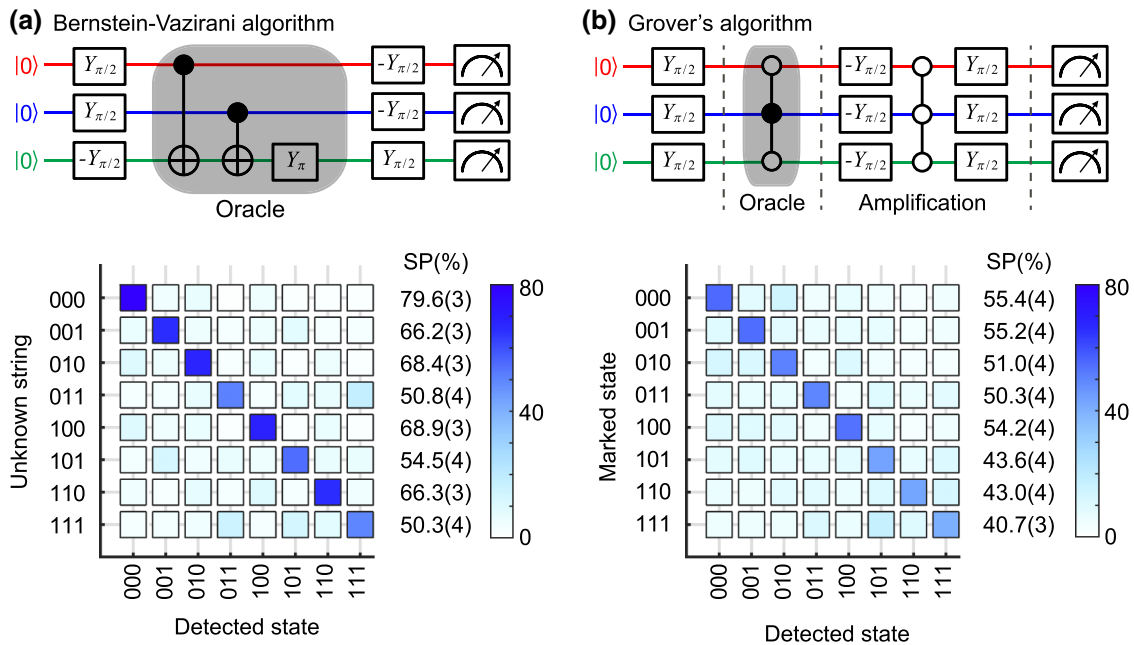


FIG. 4. Three-qubit implementations of the Bernstein-Vazirani and Grover's algorithms and their results. (a) The gray area represents the circuit diagram for the oracle implementation. The particular oracle is showing the realization of the unknown string "111," while the string "000" can be realized by application of no gates. The bottom panel shows experimental outcomes indicating success probabilities. The theoretically expected SPs are 100% for all cases. (b) The oracle for Grover's algorithm is realized by the application of CCZ gates (connected black and white circles; black representing 1 and white representing 0) conditioned on different qubit states. The probability amplification is performed by a  $CCZ_{000}$  gate (which flips the phase of  $|000\rangle$ ) sandwiched between single-qubit  $-\pi/2$  and  $+\pi/2$  rotations about the  $y$  axis on all the qubits. The bottom panels show SPs for each marked state. Ideal values for a single iteration are 78.125%. Each of the oracle implementations are repeated 20 000 times for both algorithms. The numbers in parentheses represent the standard error of the outcomes.

the answer. Note that our circuit is significantly simpler than the conventional circuit [1,21], because of access to generalized CCZ gates (that can flip phase for any combination of  $|0\rangle$  or  $|1\rangle$  as controls). The outcomes for the eight possible oracles are shown in Fig. 4(b) with mean SP of 49.2(4)%. These results are significantly better than a recent demonstration in the trapped-ion system [21] with a mean SP of 38.7% and moderately better than IBM's quantum processors on the cloud, where we obtain a mean SP of 44.9% (tested using the best three qubits with all-to-all connectivity on a five-qubit processor, see Appendix H). Another algorithm that can be implemented efficiently by utilizing the virtual  $CC\theta$  gates is the quantum Fourier transform and we present the results in Appendix I. Our results are primarily limited by measurement errors and the current inefficient implementation of single-qubit gates and we discuss possible solutions in the next section.

#### IV. DISCUSSION

Measurement error (mean error 10.5%) due to relatively large overlaps between histograms (see Fig. 6 in Appendix E) is one of the two main factors currently limiting the performance of the trimon processor. In the current experiment, measurement fidelity is limited by the relatively small dispersive shifts of the qubits (Table I). Simulations suggest that the dispersive shifts can be made double or even more through elongation of the capacitor pads to increase dipole moment. The challenge is to achieve this while ensuring certain asymmetry in the capacitance matrix for retaining optimal level spacing. The measurement can be further improved by exploiting the quantum nondemolition nature of the readout to get the full three-bit measurement result in a single experimental run (as opposed to four now). In this case, after the first round of measurement, without repeating the same experiment, one can apply the relevant CCNOT gates and measure, followed by the other set of CCNOT gates and so on. This requires increasing the speed of measurements to prevent decoherence effects from spoiling the measurement fidelity. The second main factor limiting the performance is the large execution time for the single-qubit gates. The processor is programmed to apply the (native  $CC\mathcal{R}$ ) gates sequentially, but all the pulses for a single qubit can, in principle, be applied simultaneously by generating a multifrequency pulse addressing the four relevant transitions. This will reduce the execution time significantly for the single-qubit gates and improve the performance of the processor.

Other possible improvements in trimon's performance can come from combining faster Rabi drives with appropriate pulse shaping or optimal control techniques [50,51]. We are presently exploring all these solutions to improve the performance of our processor in future experiments.

#### V. SUMMARY AND OUTLOOK

In summary, we present a universally programmable solid-state three-qubit processor with native high-fidelity three-qubit gates in superconducting architecture. Our results clearly illustrate the flexibility of the system and efficient ways of implementing various algorithms by exploiting the native three-qubit gates. We envisage the trimon as a building block for larger systems where multiple trimons can be coupled using bus cavities and intertrimon gates are performed by adapting the well-established techniques of cross-resonance [52,53]. This helps in realizing a small-scale processor with enhanced connectivity resulting in more efficient implementation of algorithms. Another possible approach is to build circuits with a larger number of junctions in the loop (multimons [36]) to implement all-to-all coupled multiqubit systems. Such systems could have applications in adiabatic quantum computing [54] and in efficiently simulating arbitrary Hamiltonians ( $n \times n$  matrix with real entries) using the single-excitation subspace of the  $n$ -qubit system without requiring any error correction [55,56].

#### ACKNOWLEDGMENTS

This work is supported by the Department of Atomic Energy of the Government of India. R.V. acknowledges support from the Department of Science and Technology, India via the Ramanujan Fellowship and Nanomission. We thank Anirban Bhattacharjee for help with numerical simulations and Pranab Sen for useful discussions. We acknowledge the TIFR nanofabrication facility. We also acknowledge use of the IBM Q for this work.

#### AUTHOR CONTRIBUTIONS

T.R. and S.H. designed the device. S.H., M.C., and M.P.P. fabricated the device. T.R. designed the experimental protocols and performed simulations. T.R. and S.K. performed the experiments and T.R. analyzed the data. S.H. developed the MLE code for density matrix reconstruction. T.R., S.H., and R.V. wrote the manuscript with inputs from co-authors. R.V. conceived and supervised the whole project.

#### APPENDIX A: CLASSICAL BOUNDS FOR DIFFERENT QUANTUM ALGORITHMS

We want to compute the maximum classical success rates for problems addressed by Deutsch-Jozsa [37], Bernstein-Vazirani [38], and Grover's [39] algorithm for one iteration of the functional evaluation. In the first case, given a specific output, the chance of the function being balanced or constant is exactly half. Therefore, the best strategy is to guess the function randomly, resulting in a success rate of 50%.

A single functional evaluation using a classical circuit for the determination of an unknown string  $\mathbf{c}$  can, at maximum, reveal one bit of information. Hence, if  $\mathbf{c}$  is a string of three bits, the other two bits have to be chosen randomly. Therefore, the probability of success in this case is  $\frac{1}{2} \cdot \frac{1}{2} = 25\%$ .

The optimal classical strategy for searching an unsorted database (of size  $2^3 = 8$ ) provides the correct answer with a probability of  $\frac{1}{8} + \frac{7}{8} \cdot \frac{1}{7} = 25\%$ . This result corresponds to a chance of  $\frac{1}{8}$  getting the right outcome in the first iteration, followed by a random guess in case the first query failed.

## APPENDIX B: DEVICE PARAMETERS

It is important to choose the device parameters in such a way that all transitions in the level diagram [see Fig. 2(a) in the main text] are well separated from each other for fast gate operations and prevention of leakage out of logical subspace. Another important criterion is to ensure that the absolute energy of the  $|111\rangle$  levels is significantly smaller than the available potential height of  $4E_{J_{\min}}$  set by the smallest of the four junctions [36]. In order to find the required device parameters, we first start with a set of guess parameters and a target level diagram where each transition is separated by at least 30 MHz from any other transition. Then we run a minimization routine (downhill simplex) using the method described in Ref. [36] to find the Josephson-junction energies and capacitances constrained to feasible values. A finite-element simulation (using COMSOL®) is used to find the geometric structure that gives rise to the required capacitance values. Josephson energies for different junctions are converted into junction overlap dimensions from independent fabrication calibrations. Finally, the device is prepared using standard lithographic and electron-beam evaporation techniques. For the device we present here, required asymmetries are put in the capacitor structure while keeping the junctions identical to minimize fabrication uncertainties, which are prominent for smaller features. Further, two of the diagonally opposite junctions are replaced with SQUIDs [see Fig. 1 in the main text] for *in situ* control of the junctions asymmetry to play with the level spacings. An added advantage of making the trimon asymmetric is that all the three modes now have moderately strong coupling to the host readout cavity (due to the presence of a dipolar component along the resonator's electric field of the  $TE_{101}$  mode). Consequently, we need lower power to drive modes B and C, leading to negligible ac Stark shifts on the other modes. This simplifies the overall calibration of gates significantly.

After experimental determination of the frequencies, interqubit coupling strengths, and anharmonicities, one can use the same minimization tool to predict the device parameters that would have led to the properties observed.

For the device presented here, the best fit parameters are  $E_{J_{12}} = 7.49$  GHz,  $E_{J_{23}} = 6.88$  GHz,  $E_{J_{34}} = 7.40$  GHz,  $E_{J_{41}} = 6.43$  GHz,  $C_{12} = 37.95$  fF,  $C_{23} = 34.30$  fF,  $C_{34} = 32.91$  fF,  $C_{41} = 27.53$  fF,  $C_{13} = 10.84$  fF,  $C_{24} = 19.19$  fF, where the nodes are numbered anticlockwise starting from the top pad. Ground capacitances are assumed to be 0.01 and 0.02 fF for the smaller and larger pads, respectively. To achieve the optimal level spacing we operate at a flux bias that corresponds to an integer multiple of the flux quantum for the ring but fractional flux quantum for the small SQUID loops. This operating point is evident from the observation that bottom-left ( $E_{J_{23}}$ ) and top-right ( $E_{J_{41}}$ ) junctions have smaller Josephson energies than the rest. The remaining asymmetries in the junction energies can be attributed to fabrication uncertainties (approximately 3%). The capacitance values are in good agreement (approximately 3% mismatch) with the estimates from the COMSOL® simulation.

## APPENDIX C: SIGNAL GENERATION AND MEASUREMENT SETUP

The detailed measurement setup is shown in Fig. 5. We use four microwave sources—three for the qubits and one for the readout. Pulses at the four different frequencies for a single qubit are generated by modulating a microwave tone kept close to the mean of two extreme transition frequencies. Two channels of an arbitrary waveform generator (AWG) running at  $2 \times 10^9$  samples/s are used for the sideband modulation of each qubit. We use two four-channel AWGs, one of them being triggered by the master AWG. Modulating waveforms sent to two AWGs are generated with appropriate time shifts to account for the trigger delay and synchronize the outputs. Input signals are passed through a 20-dB attenuator (at 4-K stage) followed by reflective low-pass and lossy Eccosorb® filters [57] attached to the base plate. The trimon device is placed inside a copper 3D rectangular cavity with resonant frequency  $\omega_r/2\pi = 7.2742$  GHz ( $TE_{101}$  mode). Qubit state preparation and joint dispersive readout are performed by sending microwave tones through a common input coaxial line. The transmitted signal at  $\omega_r$  is first amplified using a near-quantum-limited Josephson parametric amplifier [58] followed by a commercial HEMT amplifier at 4 K and room-temperature amplifiers. The homodyne detection of the outgoing signal is performed by demodulation, further amplification and digitization at a rate of  $100 \times 10^6$  samples/s. The digitized signal is stored and processed inside a computer.

## APPENDIX D: RANDOMIZED BENCHMARKING

We estimate the gate fidelity corresponding to a particular transition by carrying out Clifford-based standard randomized benchmarking in the two-level subspace corresponding to that transition. We call this the transition

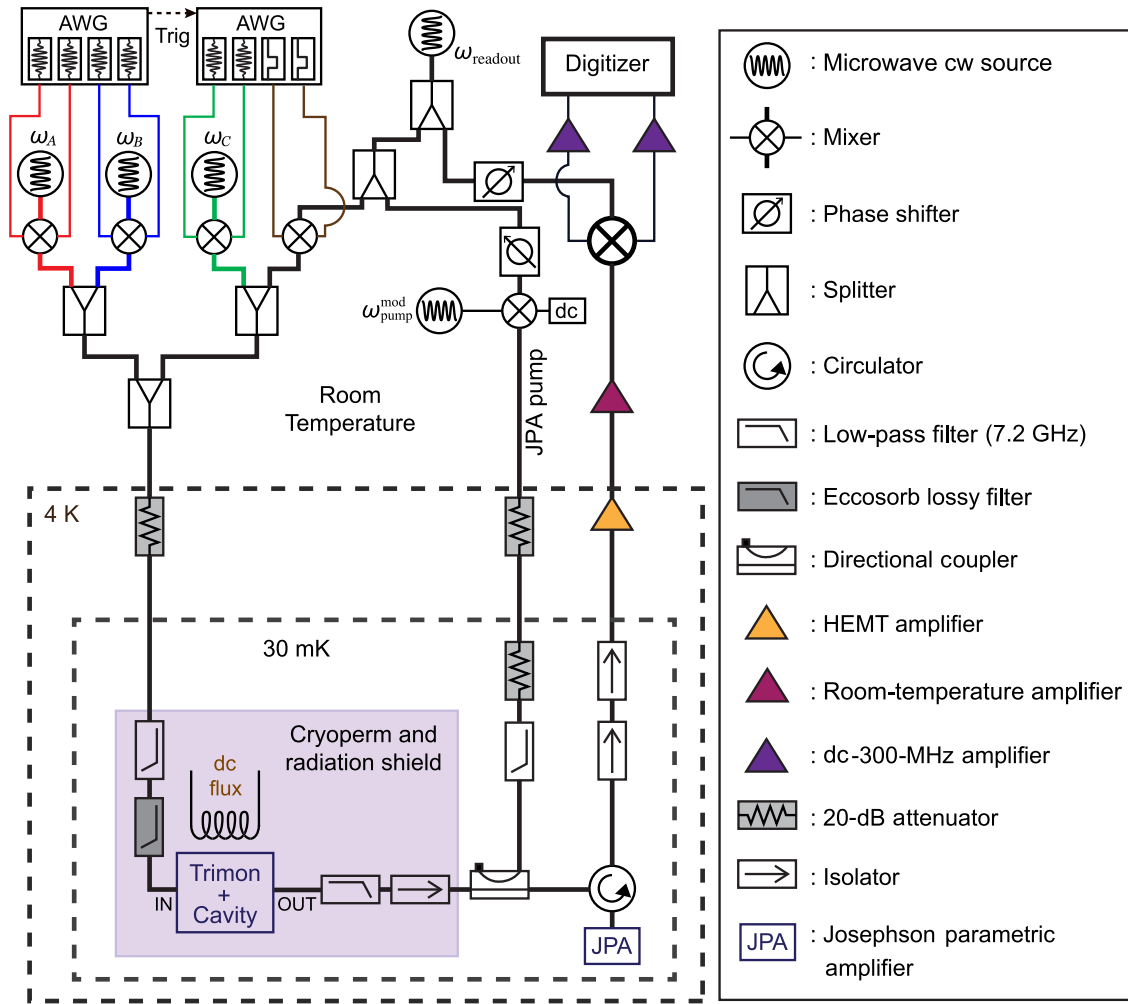


FIG. 5. Room temperature and cryogenic circuitry for the three-qubit measurement setup.

selective RB. In this protocol we choose a group of rotations that maps the two-level system between two polar and four equally spaced equatorial points on the Bloch sphere. We arrange them in a random fashion to remove any bias from the gate error. Finally, we apply a recovery pulse, which is inverse of the effective rotation due to all previous gates of that sequence. We do a projective measurement on the final state. The initial state population at the end of the sequence is defined as the sequence fidelity. As we vary the length ( $N_s$ ) of the sequences, error accumulation gives rise to an exponential decay of the sequence fidelity  $\mathcal{F}_s$ , which follows as  $\mathcal{F}_s = Ap_s^{N_s} + B$ . The SPAM error affects only  $A$  and  $B$  and leaves the decay rate  $p_s$  unaffected. The average gate fidelity  $\mathcal{F}_{\text{avg}}$  is then obtained from  $\mathcal{F}_{\text{avg}} = (1 + p_s)/2$ .

To quantify the error in a particular gate  $\mathcal{G}$ , we first obtain a reference curve by performing standard RB and extract the decay rate  $p_{\text{ref}}$ . Now we interleave the target gate  $\mathcal{G}$  between the randomly generated Cliffords and fit the decay curve to another exponential of the same form

resulting in a decay rate  $p_{\mathcal{G}}$ . The error of the target gate can be estimated by separating out the error due to the reference RB using the formula,  $r_{\mathcal{G}} = (1 - p_{\mathcal{G}}/p_{\text{ref}})/2$ . Fidelity  $\mathcal{F}_{\mathcal{G}}$  of the gate  $\mathcal{G}$  is then obtained from  $\mathcal{F}_{\mathcal{G}} = 1 - r_{\mathcal{G}}$ .

In order to execute RB addressing a particular transition in the full three-qubit Hilbert space, we first initialize the system to the lower-energy state of that particular two-level subspace. This might require zero, one or two additional CCNOT pulses depending on the particular transition. Every RB sequence is appended with pulses that will bring the system back to  $|000\rangle$  before the final projective measurement. The sequence fidelity is then measured by the population of the  $|000\rangle$  state. For every RB experiment, we vary the sequence length  $N_s$  from 1 to 40 and for every given length ten random Clifford sequences are chosen. The fidelity of each such sequence is estimated by performing 30 000 repetitions. The average Clifford gate fidelities and the generalized Toffoli  $[CCR(-\pi/2, \pi)]$  gate fidelities obtained from standard and interleaved RB for all the transitions are tabulated in Table III.



TABLE III. Average gate fidelities  $\mathcal{F}_{\text{avg}}$  and generalized Toffoli gate fidelities  $\mathcal{F}_{\pi}$  at the 12 transitions obtained from standard and interleaved randomized benchmarking experiments, respectively. The numbers in the parentheses represent fitting error. Transition frequencies and  $\pi$ -pulse lengths are also tabulated.

Transition	$\omega/2\pi$ (GHz)	$\mathcal{F}_{\text{avg}}$	$\mathcal{F}_{\pi}$	$\pi$ pulse (ns)
AB0C0	4.9278	0.994(2)	0.999(2)	125
AB0C1	4.6858	0.988(2)	0.989(1)	226
AB1C0	4.7355	0.993(1)	0.993(1)	230
AB1C1	4.4837	0.978(1)	0.985(1)	316
BC0A0	4.5146	0.992(2)	0.996(1)	617
BC0A1	4.3222	0.989(1)	0.995(1)	257
BC1A0	4.3032	0.981(1)	0.983(1)	293
BC1A1	4.1011	0.980(1)	0.984(1)	333
CA0B0	5.6864	0.992(1)	0.992(1)	319
CA0B1	5.4750	0.989(1)	0.994(1)	311
CA1B0	5.4444	0.986(1)	0.992(1)	295
CA1B1	5.2232	0.982(1)	0.986(1)	333

### APPENDIX E: QUBIT READOUT AND STATE TOMOGRAPHY

Since all the three qubits share the same host cavity, they are subject to joint dispersive readout [13,43–45]. Typical histograms of all the basis states resulting from a  $\sigma_z$  measurement are shown in Fig. 6. Although large overlaps between some basis states appear because of similar dispersive shifts (see Table I in the main text), states  $|000\rangle$  and  $|111\rangle$  have very small overlap with the rest and can be measured with high confidence. We draw two demarcation lines (dashed gray lines in Fig. 6) to separate states  $|000\rangle$  and  $|111\rangle$  from the rest. Consequently, any particular outcome will fall into three categories: “000” (if on the left of the left demarcation line), “111” (if on the right of the right demarcation line) or “Neither” (if in between the two demarcation lines). In any experimental run we discard the “Neither” outcomes as those belong to the rest

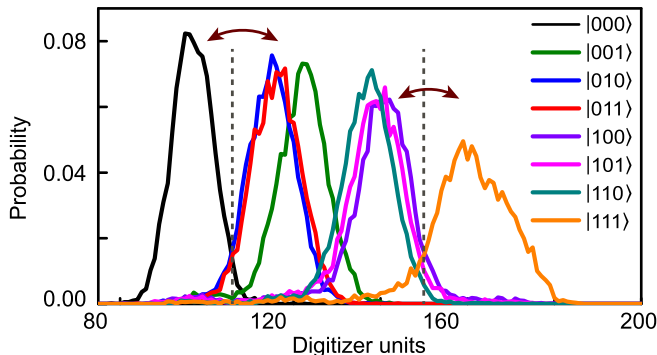


FIG. 6. Typical histograms obtained from the  $\sigma_z$  measurement of the basis states for a trimon. Two demarcation (dashed gray) lines can be drawn to distinguish states  $|000\rangle$  and  $|111\rangle$  from the rest. Then appropriate CNOT gates are applied to find projections along other basis directions.

of the six possible basis states. Thus, in the first measurement, one finds projections along  $|000\rangle$  and  $|111\rangle$ . Then to find projections along  $|001\rangle$  and  $|110\rangle$ , we repeat the same experiment but two CCNOT gates are applied at frequencies  $\omega_{CA0B0}$  and  $\omega_{CA1B1}$  to exchange population between pairs  $|000\rangle \leftrightarrow |001\rangle$  and  $|110\rangle \leftrightarrow |111\rangle$  before the final readout. In the next iteration, two other CCNOT gates are applied to perform measurements along  $|010\rangle$  and  $|101\rangle$  and so on. One thus needs four rounds of measurements to find projections of all three qubits along the  $\sigma_z$  direction. Measurement errors for the states  $|000\rangle$  and  $|111\rangle$  obtained from the extreme two histograms in Fig. 6 are  $\mathcal{E}_{000} = 4.9(2)\%$  and  $\mathcal{E}_{111} = 14.8(3)\%$ , respectively. Note that there are two sources of error—(a) part of the histogram that falls outside the binning window and (b) the tails of other histograms that fall inside the binning window (false positives). In order to obtain measurement errors for other basis states, errors for the relevant CCNOT gates used for the swap operations are to be added.

### APPENDIX F: TOMOGRAPHY AND FIDELITY OF VARIOUS STATES

Apart from the quantum algorithms presented in the main text, we prepare various entangled and product states and perform three-qubit tomography for verification. Performing tomography on an arbitrary state requires measurement along  $x, y, z$  axes of all qubits, i.e., along  $3 \times 3 \times 3 = 27$  orthogonal directions. This is done by applying all combinations of prerotations on individual qubits along  $x$  or  $y$  axes before performing  $\sigma_z$  measurement to find all the necessary projections. Then these projections are used to reconstruct the most probable density matrix  $\rho_{\text{expt}}$  using the maximum-likelihood estimation technique [59–61]. The fidelity of the reconstructed state is calculated using the definition  $\mathcal{F}_{\text{expt}} = \text{Tr}[\sqrt{\sqrt{\rho_{\text{th}}}\rho_{\text{expt}}\sqrt{\rho_{\text{th}}}}]$ , where  $\rho_{\text{th}}$  is the ideal density matrix corresponding to the state. The fidelities of the states prepared, along with the

TABLE IV. State fidelities obtained experimentally ( $\mathcal{F}_{\text{expt}}$ ) and from numerical simulation ( $\mathcal{F}_{\text{sim}}$ ) of various two-, three-qubit entangled, and equal superposition states along with the number of pulses required for preparation. The numbers inside the parentheses represent fidelity error obtained from bootstrapping.

Name	State	Pulses	$\mathcal{F}_{\text{expt}}(\%)$	$\mathcal{F}_{\text{sim}}(\%)$
Bell	$\frac{ 000\rangle +  111\rangle}{\sqrt{2}}$	2	95.3(1)	96.7
GHZ	$\frac{ 000\rangle + i 111\rangle}{\sqrt{2}}$	3	93.4(1)	95.1
Werner	$\frac{ 100\rangle +  010\rangle +  001\rangle}{\sqrt{3}}$	3	95.4(1)	96.5
Equal superposition	$\frac{( 0\rangle +  1\rangle)^{\otimes 3}}{2\sqrt{2}}$	7	93.3(1)	95.9

number of native pulses required for preparation are tabulated in Table IV. These fidelity numbers are corrected for measurement errors due to histogram overlaps (see Appendix G). In order to characterize the performance of our processor, we also perform numerical simulations using the QuTiP open-source software package [62,63] with the decoherence parameters shown in Table I in the main text. The fidelities  $\mathcal{F}_{\text{sim}}$  are very close to what we obtain experimentally. The small discrepancy can be attributed to measurement errors, which are not included in the simulations.

### APPENDIX G: MEASUREMENT ERROR MITIGATION

We consider a model where the states are prepared with perfection and all the error is attributed to the measurement. In an error-free setup the probability  $P(i|j)$  of measuring a basis state  $i$  when a basis state  $j$  is prepared is zero if  $i \neq j$ . However, any real experimental setup deviates from this ideal behavior due to the presence of noise and/or systematic error. Our goal is to first characterize this error and then perform corrections (when appropriate) to eliminate it.

In order to perform measurement error mitigation, we prepare each of the  $2^3 = 8$  possible basis states  $j$  a large number of times, followed by immediate measurements. From the measurement histograms (counts for each possible outcome  $i$ ), we compute the error matrix  $\vec{M}$  where the elements  $M_{ij} = P(i|j)$ . In other words, the  $j$ th column of  $\vec{M}$  represents the probability of obtaining different outcomes  $i$  when the basis state  $j$  is prepared. Now, consider a state  $|\psi\rangle$  whose ideal probability distribution after a  $\sigma_z$  measurement is given by the column vector  $\vec{P}_{\text{id}}$  (consists of eight elements). The measurement error results in a modified probability distribution  $\vec{P}_{\text{expt}}$ , which is related to the ideal values as  $\vec{P}_{\text{expt}} = \vec{M} \vec{P}_{\text{id}}$ . Therefore, given the experimental outcomes  $\vec{P}_{\text{expt}}$ , the correct probability distribution can be obtained by inverting the error matrix as  $\vec{P}_{\text{id}} = \vec{M}^{-1} \vec{P}_{\text{expt}}$ . The ideal distribution  $\vec{P}_{\text{id}}$  can then be used to reconstruct the state  $|\psi\rangle$ .

### APPENDIX H: GROVER'S ALGORITHM ON IBM Q

We test the ancilla-free version of the three-qubit Grover's search on IBM's "ibmq\_5\_yorktown-ibmqx2" processor [64], which has five qubits. We use the qubits labeled as  $q[0]$ ,  $q[1]$ , and  $q[2]$  as that subset has all-to-all connectivity (the same set is used for testing the QFT algorithm discussed in the next section). The gate decomposition is shown in Fig. 7, where  $T = \begin{pmatrix} 1 & 0 \\ 0 & e^{i\pi/4} \end{pmatrix}$  is known as the  $\pi/8$  gate. We perform a single iteration of Grover's search several times (each time having 4096 shots) and depict the best result in Fig. 7. The average

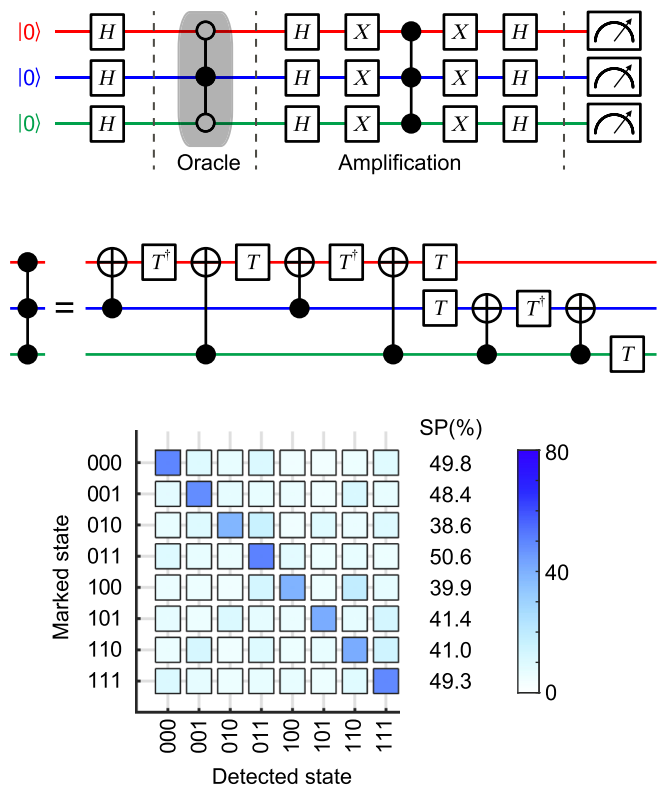


FIG. 7. Grover's algorithm implemented on IBM's "yorktown-ibmqx2" processor. The top panel shows the quantum circuit for the three-qubit Grover's search. The middle panel illustrates the decomposition of the  $CCZ_{111}$  gate. Different instances of the oracle are implemented by sandwiching  $CCZ_{111}$  gate between  $X$  gates on appropriate qubits. The bottom panel shows the probability distribution after 4096 shots for each oracle and the success probability of getting the correct answer.

success probability is 44.9%, which varied by about 5% between different runs.

### APPENDIX I: QUANTUM FOURIER TRANSFORM

As an additional example of native three qubit gates in the trimon, we implement the quantum Fourier transform, which is a key ingredient in many quantum algorithms that exploit parallel functional evaluation through preparation of a superposition state to achieve exponential speedup over classical algorithms [1]. Two such algorithms are *order finding* and *phase estimation*. Order-finding protocol plays a crucial role in Shor's factorizing algorithm [65] and the phase-estimation protocol determines the phase  $\phi$  of an eigenvalue problem  $\hat{A}|\phi\rangle = e^{i\phi}|\phi\rangle$  with  $n$ -bit precision using an  $n$ -qubit QFT [1].

The quantum circuit for the three-qubit QFT is shown in Fig. 8(a) consisting of 12 native gates (each single-qubit gate composed of four  $CC\mathcal{R}$  gates) and three virtual arbitrary controlled-phase [ $C\theta(\theta)$ ] gates [each composed of two  $CC\theta(\theta)$  gates, e.g.,  $C\theta_{A1C1}(\pi/4) = CC\theta_{A1B0C1}(\pi/4) \times$

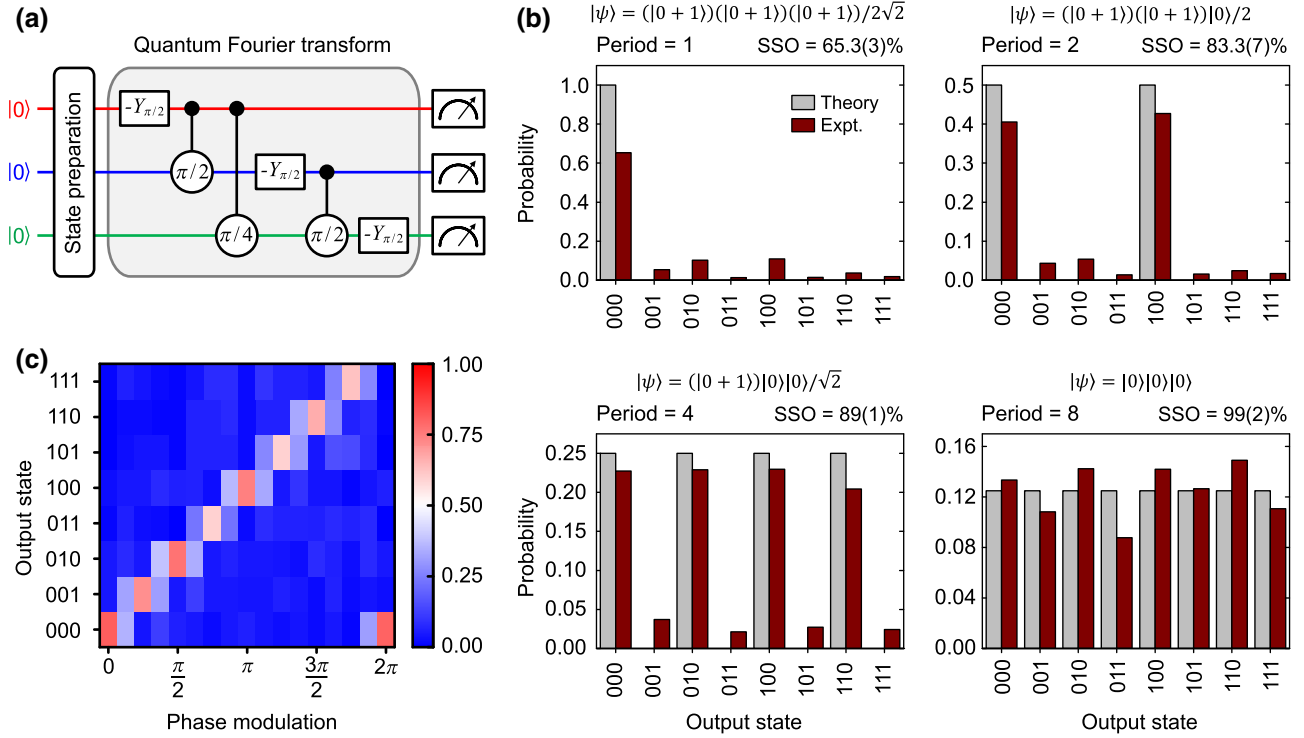


FIG. 8. Three-qubit quantum Fourier transform (QFT) protocol and results. (a) The quantum circuit for performing QFT. The state preparation step consists of single-qubit rotations to achieve desired periodicity in the coefficients  $C_j$  in  $|\psi\rangle = \sum_{j=0}^7 C_j |j\rangle$ . The gray area represents the implementation of the QFT circuit using 12 native pulses (for  $-Y_{\pi/2}$  gates) and three virtual  $C\theta$  gates. The registers are finally measured to obtain the state populations. (b) Results of the period-finding protocol for four different initial states with amplitude periodicities 1, 2, 4, and 8. The gray and brown bars represent theoretical and experimentally obtained values. The squared statistical overlap (SSO) denotes the fidelity of the process with statistical uncertainties obtained from 20 000 repetitions. (c) Results of the phase-estimation protocol. Modulating phase is swept over a range of 0 to  $2\pi$  in steps of  $2\pi/16$ . Mean fidelity obtained is 81.3(9)%.

$C\theta_{A1B1C1}(\pi/4)$ . Our QFT implementation clearly benefits from the virtual  $C\theta(\theta)$  gates without any need for deconstruction using multiple single- and two-qubit gates [66]. Note that the Hadamard gates are replaced with  $-Y_{\pi/2}$  gates, which lead to identical projections on subsequent measurement and the swap between qubits A and C is done in software after recording the outcomes. The analysis and presentation for the order-finding and phase-estimation algorithms are based on previous work in a five-qubit trapped-ion [2] system and a three-qubit NMR [16] system for ease of comparison.

### 1. Period-finding protocol

To demonstrate the period-finding protocol, we initialize the system in a superposition state of the form  $|\psi\rangle = \sum_{j=0}^7 C_j |j\rangle$ , where coefficients  $C_j$  are chosen to exhibit amplitude periodicities 1, 2, 4, and 8 [see Fig. 8(b)]. After performing the QFT, amplitude modulation appears in the distribution of state populations. To compare the results with the theoretical predictions, we define squared statistical overlap [16] as  $SSO = \left( \sum_{j=0}^{N-1} \sqrt{t_j} e_j \right)^2$ , where  $t_j$

and  $e_j$  are the theoretically expected and experimentally obtained probabilities, respectively, for state  $|j\rangle$ . The SSOs for each input state are shown in Fig. 8(b), with an average of 84(1)%. The performance is similar to previous demonstration of 83.6% in a trapped-ion system [2] (five-qubit algorithm) and somewhat poorer than 91.8% obtained on IBM’s quantum processor (three-qubit algorithm). Note that we use the built-in Hadamard (“H”) and controlled-Z-rotation (“cRz”) gates to implement the QFT circuit in Fig. 8(a) on the IBM system.

### 2. Quantum phase estimation

The phase-estimation protocol is identical to that of the period-finding protocol, where the input state is prepared in the form  $|\psi\rangle = \frac{1}{2\sqrt{2}} \otimes_{k=0}^2 (|0\rangle + e^{-i2^k \phi} |1\rangle)$ . Preparation of these states requires rotation of each qubit about the Z axis and  $|\psi\rangle$  exhibits  $\phi$ -dependent phase modulation in the coefficients  $C_k$ . Performing QFT on this state allows determination of  $\phi$  with a three-bit precision, which is mapped onto the population of the states. We swept  $\phi$  from 0 to  $2\pi$  in steps of  $2\pi/16$  and the results are shown in Fig. 8(c).

Values of  $\phi$  that are integer multiples of  $2\pi/8$  result in the state  $|8\phi/2\pi\rangle$  after the QFT, whereas for noninteger multiples the value of  $\phi$  is mapped on to nearest three-bit states. The average success probability for the cases of integer multiples is 70.1(3)% and the mean SSO for the noninteger multiples is 92(1)%. These results are again similar to the state-of-the-art implementation in the trapped-ion system [2] (five-qubit algorithm) with 61.9(5)% for integer multiples and IBM's quantum processor (three-qubit algorithm) with 70.1% success probability for integer and 92.0% SSO for noninteger multiples.

- 
- [1] Michael A. Nielsen and Isaac L. Chuang, *Quantum Computation and Quantum Information* (Cambridge University Press, Cambridge, UK, 2010).
- [2] S. Debnath, N. M. Linke, C. Figgatt, K. A. Landsman, K. Wright, and C. Monroe, Demonstration of a small programmable quantum computer with atomic qubits, *Nature* **536**, 63 (2016).
- [3] Abhinav Kandala, Antonio Mezzacapo, Kristan Temme, Maika Takita, Markus Brink, Jerry M. Chow, and Jay M. Gambetta, Hardware-efficient variational quantum eigensolver for small molecules and quantum magnets, *Nature* **549**, 242 (2017).
- [4] K. Wright *et al.*, Benchmarking an 11-qubit quantum computer, *Nat. Commun.* **10**, 5464 (2019).
- [5] Frank Arute, Kunal Arya, Ryan Babbush, Dave Bacon, Joseph C. Bardin, Rami Barends, Rupak Biswas, Sergio Boixo, Fernando GSL Brandao, David A. Buell *et al.*, Quantum supremacy using a programmable superconducting processor, *Nature* **574**, 505 (2019).
- [6] John Preskill, Quantum computing in the NISQ era and beyond, *Quantum* **2**, 79 (2018).
- [7] Adriano Barenco, Charles H. Bennett, Richard Cleve, David P. DiVincenzo, Norman Margolus, Peter Shor, Tycho Sleator, John A. Smolin, and Harald Weinfurter, Elementary gates for quantum computation, *Phys. Rev. A* **52**, 3457 (1995).
- [8] Noah Linden, Hervé Barjat, and Ray Freeman, An implementation of the Deutsch–Jozsa algorithm on a three-qubit NMR quantum computer, *Chem. Phys. Lett.* **296**, 61 (1998).
- [9] Lieven M. K. Vandersypen, Matthias Steffen, Gregory Breyta, Costantino S. Yannoni, Mark H. Sherwood, and Isaac L. Chuang, Experimental realization of Shor's quantum factoring algorithm using nuclear magnetic resonance, *Nature* **414**, 833 (2001).
- [10] Stephan Gulde, Mark Riebe, Gavin P. T. Lancaster, Christoph Becher, Jürgen Eschner, Hartmut Häffner, Ferdinand Schmidt-Kaler, Isaac L. Chuang, and Rainer Blatt, Implementation of the Deutsch–Jozsa algorithm on an ion-trap quantum computer, *Nature* **421**, 48 (2003).
- [11] E. Brainis, L.-P. Lamoureux, N. J. Cerf, Ph. Emplit, M. Haelterman, and S. Massar, Fiber-Optics Implementation of the Deutsch–Jozsa and Bernstein–Vazirani Quantum Algorithms with Three Qubits, *Phys. Rev. Lett.* **90**, 157902 (2003).
- [12] K.-A. Brickman, P. C. Haljan, P. J. Lee, M. Acton, L. Deslauriers, and C. Monroe, Implementation of Grover's quantum search algorithm in a scalable system, *Phys. Rev. A* **72**, 050306 (2005).
- [13] L. DiCarlo, J. M. Chow, J. M. Gambetta, Lev S. Bishop, B. R. Johnson, D. I. Schuster, J. Majer, A. Blais, L. Frunzio, S. M. Girvin, and R. J. Schoelkopf, Demonstration of two-qubit algorithms with a superconducting quantum processor, *Nature* **460**, 240 (2009).
- [14] Fazhan Shi, Xing Rong, Nanyang Xu, Ya Wang, Jie Wu, Bo Chong, Xinhua Peng, Juliane Kniepert, Rolf-Simon Schoenfeld, Wolfgang Harneit, Mang Feng, and Jiangfeng Du, Room-Temperature Implementation of the Deutsch–Jozsa Algorithm with a Single Electronic Spin in Diamond, *Phys. Rev. Lett.* **105**, 040504 (2010).
- [15] Thomas Monz, Daniel Nigg, Esteban A. Martinez, Matthias F. Brandl, Philipp Schindler, Richard Rines, Shannon X. Wang, Isaac L. Chuang, and Rainer Blatt, Realization of a scalable Shor algorithm, *Science* **351**, 1068 (2016).
- [16] J. Chiaverini, J. Britton, D. Leibfried, E. Knill, M. D. Barrett, R. B. Blakestad, W. M. Itano, J. D. Jost, C. Langer, R. Ozeri, T. Schaetz, and D. J. Wineland, Implementation of the semiclassical quantum fourier transform in a scalable system, *Science* **308**, 997 (2005).
- [17] Y. Salathé, M. Mondal, M. Oppliger, J. Heinsoo, P. Kurpiers, A. Potočnik, A. Mezzacapo, U. Las Heras, L. Lamata, E. Solano, S. Filipp, and A. Wallraff, Digital Quantum Simulation of Spin Models with Circuit Quantum Electrodynamics, *Phys. Rev. X* **5**, 021027 (2015).
- [18] R. Barends *et al.*, Digitized adiabatic quantum computing with a superconducting circuit, *Nature* **534**, 222 (2016).
- [19] Erik Lucero, R. Barends, Y. Chen, J. Kelly, M. Mariantoni, A. Megrant, P. O'Malley, D. Sank, A. Vainsencher, J. Wenner, T. White, Y. Yin, A. N. Cleland, and John M. Martinis, Computing prime factors with a Josephson phase qubit quantum processor, *Nat. Phys.* **7**, 819 (2012).
- [20] R. Barends *et al.*, Digital quantum simulation of fermionic models with a superconducting circuit, *Nat. Commun.* **6**, 7654 (2015).
- [21] C. Figgatt, D. Maslov, K. A. Landsman, N. M. Linke, S. Debnath, and C. Monroe, Complete 3-qubit Grover search on a programmable quantum computer, *Nat. Commun.* **8**, 1918 (2017).
- [22] Abhinav Kandala, Kristan Temme, Antonio D. Córcoles, Antonio Mezzacapo, Jerry M. Chow, and Jay M. Gambetta, Error mitigation extends the computational reach of a noisy quantum processor, *Nature* **567**, 491 (2019).
- [23] Tommaso Toffoli, in *Automata, Languages and Programming*, edited by Jaco de Bakker and Jan van Leeuwen (Springer Berlin Heidelberg, Berlin, Heidelberg, 1980), pp. 632–644.
- [24] Yaoyun Shi, Both Toffoli and controlled-NOT need little help to do universal quantum computing, *Quantum Info. Comput.* **3**, 84 (2003).
- [25] D. G. Cory, M. D. Price, W. Maas, E. Knill, R. Laflamme, W. H. Zurek, T. F. Havel, and S. S. Somaroo, Experimental Quantum Error Correction, *Phys. Rev. Lett.* **81**, 2152 (1998).
- [26] Arkady Fedorov, Lars Steffen, Matthias Baur, Marcus P. da Silva, and Andreas Wallraff, Implementation of a Toffoli gate with superconducting circuits, *Nature* **481**, 170 (2012).

- [27] T. Monz, K. Kim, W. Hänsel, M. Riebe, A. S. Villar, P. Schindler, M. Chwalla, M. Hennrich, and R. Blatt, Realization of the Quantum Toffoli Gate with Trapped Ions, *Phys. Rev. Lett.* **102**, 040501 (2009).
- [28] Matthew D. Reed, Leonardo DiCarlo, Simon E. Nigg, Luyan Sun, Luigi Frunzio, Steven M. Girvin, and Robert J. Schoelkopf, Realization of three-qubit quantum error correction with superconducting circuits, *Nature* **482**, 382 (2012).
- [29] Leonardo DiCarlo, Matthew D. Reed, Luyan Sun, Blake R. Johnson, Jerry M. Chow, Jay M. Gambetta, Luigi Frunzio, Steven M. Girvin, Michel H. Devoret, and Robert J. Schoelkopf, Preparation and measurement of three-qubit entanglement in a superconducting circuit, *Nature* **467**, 574 (2010).
- [30] Yvonne Y. Gao, Brian J. Lester, Kevin S. Chou, Luigi Frunzio, Michel H. Devoret, Liang Jiang, S. M. Girvin, and Robert J. Schoelkopf, Entanglement of bosonic modes through an engineered exchange interaction, *Nature* **566**, 509 (2019).
- [31] Benjamin P. Lanyon, Marco Barbieri, Marcelo P. Almeida, Thomas Jennewein, Timothy C. Ralph, Kevin J. Resch, Geoff J. Pryde, Jeremy L. O'Brien, Alexei Gilchrist, and Andrew G. White, Simplifying quantum logic using higher-dimensional Hilbert spaces, *Nat. Phys.* **5**, 134 (2009).
- [32] Chao Song, Shi-Biao Zheng, Pengfei Zhang, Kai Xu, Libo Zhang, Qiujiang Guo, Wuxin Liu, Da Xu, Hui Deng, Keqiang Huang, Dongning Zheng, Xiaobo Zhu, and H. Wang, Continuous-variable geometric phase and its manipulation for quantum computation in a superconducting circuit, *Nat. Commun.* **8**, 1061 (2017).
- [33] Simon Panyella Pedersen, K. S. Christensen, and N. T. Zinner, Native three-body interaction in superconducting circuits, *Phys. Rev. Res.* **1**, 033123 (2019).
- [34] Chao Song, Kai Xu, Wuxin Liu, Chui-ping Yang, Shi-Biao Zheng, Hui Deng, Qiwei Xie, Keqiang Huang, Qiujiang Guo, Libo Zhang, Pengfei Zhang, Da Xu, Dongning Zheng, Xiaobo Zhu, H. Wang, Y.-A. Chen, C.-Y. Lu, Siyuan Han, and Jian-Wei Pan, 10-Qubit Entanglement and Parallel Logic Operations with a Superconducting Circuit, *Phys. Rev. Lett.* **119**, 180511 (2017).
- [35] Chao Song, Kai Xu, Hekang Li, Yu-Ran Zhang, Xu Zhang, Wuxin Liu, Qiujiang Guo, Zhen Wang, Wenhui Ren, Jie Hao, Hui Feng, Heng Fan, Dongning Zheng, Da-Wei Wang, H. Wang, and Shi-Yao Zhu, Generation of multicomponent atomic Schrödinger cat states of up to 20 qubits, *Science* **365**, 574 (2019).
- [36] Tanay Roy, Madhavi Chand, Anirban Bhattacharjee, Sumeru Hazra, Suman Kundu, Kedar Damle, and R. Vijay, Multimode superconducting circuits for realizing strongly coupled multiqubit processor units, *Phys. Rev. A* **98**, 052318 (2018).
- [37] David Deutsch and Richard Jozsa, Rapid solution of problems by quantum computation, *Proc. R. Soc. Lond. A: Math. Phys. Eng. Sci.* **439**, 553 (1992).
- [38] Ethan Bernstein and Umesh Vazirani, Quantum complexity theory, *SIAM J. Comput.* **26**, 1411 (1997).
- [39] Lov K. Grover, Quantum Mechanics Helps in Searching for a Needle in a Haystack, *Phys. Rev. Lett.* **79**, 325 (1997).
- [40] Tanay Roy, Suman Kundu, Madhavi Chand, Sumeru Hazra, N. Nehra, R. Cosmic, A. Ranadive, Meghan P. Patankar, Kedar Damle, and R. Vijay, Implementation of Pairwise Longitudinal Coupling in a Three-Qubit Superconducting Circuit, *Phys. Rev. Appl.* **7**, 054025 (2017).
- [41] Jens Koch, Terri M. Yu, Jay Gambetta, A. A. Houck, D. I. Schuster, J. Majer, Alexandre Blais, M. H. Devoret, S. M. Girvin, and R. J. Schoelkopf, Charge-insensitive qubit design derived from the cooper pair box, *Phys. Rev. A* **76**, 042319 (2007).
- [42] David C. McKay, Christopher J. Wood, Sarah Sheldon, Jerry M. Chow, and Jay M. Gambetta, Efficient z gates for quantum computing, *Phys. Rev. A* **96**, 022330 (2017).
- [43] D. Riste, M. Dukalski, C. A. Watson, G. De Lange, M. J. Tiggelman, Ya M. Blanter, Konrad W. Lehnert, R. N. Schouten, and L. DiCarlo, Deterministic entanglement of superconducting qubits by parity measurement and feedback, *Nature* **502**, 0 (2013).
- [44] S. Filipp, P. Maurer, P. J. Leek, M. Baur, R. Bianchetti, J. M. Fink, M. Göppl, L. Steffen, J. M. Gambetta, A. Blais, and A. Wallraff, Two-Qubit State Tomography Using a Joint Dispersive Readout, *Phys. Rev. Lett.* **102**, 200402 (2009).
- [45] J. Majer, J. M. Chow, J. M. Gambetta, Jens Koch, B. R. Johnson, J. A. Schreier, L. Frunzio, D. I. Schuster, A. A. Houck, A. Wallraff, A. Blais, M. H. Devoret, S. M. Girvin, and R. J. Schoelkopf, Coupling superconducting qubits via a cavity bus, *Nature* **449**, 443 (2015).
- [46] J. M. Chow, J. M. Gambetta, L. Tornberg, Jens Koch, Lev S. Bishop, A. A. Houck, B. R. Johnson, L. Frunzio, S. M. Girvin, and R. J. Schoelkopf, Randomized Benchmarking and Process Tomography for Gate Errors in a Solid-State Qubit, *Phys. Rev. Lett.* **102**, 090502 (2009).
- [47] Easwar Magesan, Jay M. Gambetta, B. R. Johnson, Colm A. Ryan, Jerry M. Chow, Seth T. Merkel, Marcus P. da Silva, George A. Keefe, Mary B. Rothwell, Thomas A. Ohki, Mark B. Ketchen, and M. Steffen, Efficient Measurement of Quantum Gate Error by Interleaved Randomized Benchmarking, *Phys. Rev. Lett.* **109**, 080505 (2012).
- [48] Oliver Mangold, Andreas Heidebrecht, and Michael Mehring, NMR tomography of the three-qubit Deutsch-Jozsa algorithm, *Phys. Rev. A* **70**, 042307 (2004).
- [49] Michel Boyer, Gilles Brassard, Peter Høyer, and Alain Tapp, Tight bounds on quantum searching, *Fortschr. Phys.* **46**, 493 (1998).
- [50] F. Motzoi, J. M. Gambetta, P. Rebentrost, and F. K. Wilhelm, Simple Pulses for Elimination of Leakage in Weakly Nonlinear Qubits, *Phys. Rev. Lett.* **103**, 110501 (2009).
- [51] Shavindra P. Premaratne, Jen-Hao Yeh, F. C. Wellstood, and B. S. Palmer, Implementation of a generalized controlled-not gate between fixed-frequency transmons, *Phys. Rev. A* **99**, 012317 (2019).
- [52] Jerry M. Chow, A. D. Córcoles, Jay M. Gambetta, Chad Rigetti, B. R. Johnson, John A. Smolin, J. R. Rozen, George A. Keefe, Mary B. Rothwell, Mark B. Ketchen, and M. Steffen, Simple All-Microwave Entangling Gate for Fixed-Frequency Superconducting Qubits, *Phys. Rev. Lett.* **107**, 080502 (2011).
- [53] Sumeru Hazra, Kishor V. Salunkhe, Anirban Bhattacharjee, Gaurav Bothara, Suman Kundu, Tanay Roy, Meghan P.

- Patankar, and R. Vijay, Engineering cross resonance interaction in multi-modal quantum circuits, *Appl. Phys. Lett.* **116**, 152601 (2020).
- [54] Martin Leib, Peter Zoller, and Wolfgang Lechner, A transmon quantum annealer: Decomposing many-body Ising constraints into pair interactions, *Quantum Sci. Technol.* **1**, 015008 (2016).
- [55] Michael R. Geller, John M. Martinis, Andrew T. Sornborger, Phillip C. Stancil, Emily J. Pritchett, Hao You, and Andrei Galiutdinov, Universal quantum simulation with prethreshold superconducting qubits: Single-excitation subspace method, *Phys. Rev. A* **91**, 062309 (2015).
- [56] Amara Katarawa and Michael R. Geller, Three-step implementation of any  $n \times n$  unitary with a complete graph of  $n$  qubits, *Phys. Rev. A* **92**, 032306 (2015).
- [57] D. H. Slichter, O. Naaman, and I. Siddiqi, Millikelvin thermal and electrical performance of lossy transmission line filters, *Appl. Phys. Lett.* **94**, 192508 (2009).
- [58] M. Hatridge, R. Vijay, D. H. Slichter, John Clarke, and I. Siddiqi, Dispersive magnetometry with a quantum limited squid parametric amplifier, *Phys. Rev. B* **83**, 134501 (2011).
- [59] K. Banaszek, G. M. D’Ariano, M. G. A. Paris, and M. F. Sacchi, Maximum-likelihood estimation of the density matrix, *Phys. Rev. A* **61**, 010304 (1999).
- [60] Daniel F. V. James, Paul G. Kwiat, William J. Munro, and Andrew G. White, Measurement of qubits, *Phys. Rev. A* **64**, 052312 (2001).
- [61] Z. Hradil, Quantum-state estimation, *Phys. Rev. A* **55**, R1561 (1997).
- [62] J. R. Johansson, P. D. Nation, and Franco Nori, QuTiP: An open-source python framework for the dynamics of open quantum systems, *Comput. Phys. Commun.* **183**, 1760 (2012).
- [63] J. R. Johansson, P. D. Nation, and Franco Nori, QuTiP 2: A python framework for the dynamics of open quantum systems, *Comput. Phys. Commun.* **184**, 1234 (2013).
- [64] IBM Q team, IBM Q 5 yorktown backend specification V2.0.1 (2019).
- [65] Peter W. Shor, Polynomial-time algorithms for prime factorization and discrete logarithms on a quantum computer, *SIAM Rev.* **41**, 303 (1999).
- [66] Taewan Kim and Byung-Soo Choi, Efficient decomposition methods for controlled- $R_n$  using a single ancillary qubit, *Sci. Rep.* **8**, 1 (2018).